Size-dependent plastic deformation of twinned nanopillars in body-centered cubic tungsten

Shuozhi Xu, Jacob K. Startt, Thomas G. Payne, Chaitanya S. Deo, and David L. McDowell

Size-dependent plastic deformation of twinned nanopillars in body-centered cubic tungsten

Shuozhi Xu,[1,a)] Jacob K. Startt,[1] Thomas G. Payne,[2] Chaitanya S. Deo,[1] and David L. McDowell[1,2]

[1]*GWW School of Mechanical Engineering, Georgia Institute of Technology, Atlanta, Georgia 30332-0405, USA*

[2]*School of Materials Science and Engineering, Georgia Institute of Technology, Atlanta, Georgia 30332-0245, USA*

Compared with face-centered cubic metals, twinned nanopillars in body-centered cubic (BCC) systems are much less explored partly due to the more complicated plastic deformation behavior and a lack of reliable interatomic potentials for the latter. In this paper, the fault energies predicted by two semi-empirical interatomic potentials in BCC tungsten (W) are first benchmarked against density functional theory calculations. Then, the more accurate potential is employed in large scale molecular dynamics simulations of tensile and compressive loading of twinned nanopillars in BCC W with different cross sectional shapes and sizes. A single crystal, a twinned crystal, and single crystalline nanopillars are also studied as references. Analyses of the stress-strain response and defect nucleation reveal a strong tension-compression asymmetry and a weak pillar size dependence in the yield strength. Under both tensile and compressive loading, plastic deformation in the twinned nanopillars is dominated by dislocation slip on {110} planes that are nucleated from the intersections between the twin boundary and the pillar surface. It is also found that the cross sectional shape of nanopillars affects the strength and the initial site of defect nucleation but not the overall stress-strain response and plastic deformation behavior. *Published by AIP Publishing.*
[http://dx.doi.org/10.1063/1.4982754]

I. INTRODUCTION

Nanocrystalline face-centered cubic (FCC) Cu containing nanoscale twins, either equiaxially[1–3] or epitaxially,[4–6] is known to exhibit ultrahigh strength over its twin-free counterpart while preserving an acceptable level of ductility. The superior mechanical properties of the nanotwinned Cu are attributed to both a high dislocation density and significant barriers to dislocation motion during plastic deformation.[7,8] In some nanocrystalline FCC metals, e.g., Pd, twin boundary (TB) migration is favored over dislocation gliding on slip planes that are transverse to the TBs; thus, there is a softening effect due to the presence of twins in Pd.[9] Whether a TB strengthens or softens a certain metal with respect to its twin-free counterpart also depends on its intrinsic and extrinsic dimensions, as well as the geometry.[10] For example, Deng and Sansoz[11,12] found that nanoscale twins have no intrinsic influence on the yielding behavior of Au bicrystals subject to either compression or tension. In Au nanopillars, a critical ratio of the pillar diameter to the TB spacing exists, corresponding to a transition from strain hardening to strain softening,[13] as well as one from TB-induced strengthening and softening.[12] In Cu, there is an optimal height to diameter aspect ratio for which the twinned nanopillars always have a higher yield stress than their twin-free counterparts.[14] It is

also found that nanotwinned Cu nanopillars with a square cross section exhibit a more pronounced strengthening effect due to the existence of twins than for circular cross sections.[15]

Compared with FCC systems, nanopillars in body-centered cubic (BCC) metals are much less investigated.[16] Three plastic deformation mechanisms have been identified in BCC pillars: dislocation slip, twinning, and phase transformation; the dominating mechanism in a given case varies with the lattice orientation,[17,18] loading mode,[19] and pillar cross sectional area.[20] Because of the twinning-antitwinning asymmetry and different dominant plastic deformation mechanisms, the difference in strain hardening and yield strength between tension and compression of single crystalline nanopillars is more pronounced in BCC than in FCC metals;[21,22] such a difference in BCC Mo depends on both the diameter and crystallographic orientation relative to the loading direction.[23] In terms of the yield strength, experiments[24] and DD simulations[25] showed that single crystalline BCC metals generally exhibit a weaker dependence on the pillar diameter than FCC metals, which is attributed to the combined effects of the image stress and the dislocation core structure.

Most studies in BCC systems (with the exception of Refs. 22 and 26) do not involve preexisting nanoscale twins, because their high stacking fault energy (SFE) makes it difficult to produce nanoscale twins by the growth method.[27] On the other hand, deformation twinning can be prominent in

a)Author to whom correspondence should be addressed. Electronic mail: shuozhixu@gatech.edu

plastic deformation of some nanocrystalline BCC metals.[28–31] Commonly used continuum simulations, e.g., dislocation dynamics and the crystal plasticity finite element method, are unable to capture the atomic-scale TB structure evolution which is important to model dislocation/TB interactions.[32–34] It is therefore desirable to probe the mechanical properties of nanotwinned BCC structures via atomistic simulations. To the best of our knowledge, only one recent molecular dynamics (MD) simulation[22] studied nanotwinned BCC nanopillars, which revealed a tension-compression asymmetry in the TB spacing-dependent yield strength in α-Fe. Nevertheless, many issues remain unexplored, including how this asymmetry varies with the pillar diameter, the cross sectional shape, and the existence of TBs, as well as whether this size dependence in twinned BCC nanopillars is weaker than that in FCC as in the case of single crystalline nanopillars.[24,25]

In MD, it is important for the interatomic potential to yield correct fault energies related to twinning and dislocation slip to correctly reproduce plastic deformation mechanisms. For example, one challenge in modelling dislocation slip in BCC metals at low temperatures is the difficulty of the semi-empirical potentials to accurately predict the energy barrier of dislocation kink formation.[35] Particularly for tungsten (W), one of the primary candidate structural materials in fusion reactors, there are currently more than 30 different interatomic potentials in the literature.[36] Up to this point, only a few MD studies[18,37–39] have been conducted to investigate W nanopillars, using either the original Finnis-Sinclair (FS) potential[40] or the same potential but with the short range region modified by Ackland and Thetford[41] (referred to in this paper as the AT potential). Recent density functional theory (DFT) calculations found that these two potentials predict incorrect screw dislocation core/glide path and underestimate SFEs on {110} and {112} planes,[36,42,43] as well as energies of free surfaces, vacancy migration, and self-interstitial atom formation.[36] Because these quantities are important in deformation of BCC nanopillars,[22] the question arises regarding the reliability of the FS and AT potentials in this context.

In this paper, we first calculate stacking fault and planar fault energies using DFT and two semi-empirical interatomic potentials: the AT potential and an embedded-atom method (EAM) potential recently developed by Marinica *et al.*[42] (EAM4 in Ref. 42). It is found that the EAM potential[42] provides more accurate fault energies with respect to the DFT calculations. Then, we perform MD simulations to investigate size-dependent plastic deformation of twinned nanopillars in BCC W subject to both tension and compression; a single crystal, a twinned bicrystal, and single crystalline nanopillars are also investigated as references. Compared with Ref. 22 in which nanotwinned nanopillars with a 8.5 nm × 8.5 nm square cross-section were studied, the twinned nanopillars considered in this paper have a cross section size up to 70 nm, accessible by experiments,[18,44] potentially allowing direct comparison of our simulations with *in situ* transmission electron microscopy (TEM) experiments.

II. FAULT ENERGIES CALCULATED BY DFT AND TWO SEMI-EMPIRICAL INTERATOMIC POTENTIALS

Dislocation slip and twinning in metals are directly associated with certain fault energies, including generalized stacking fault energy (GSFE) on three slip planes: {110}, {112}, and {123} planes, as well as generalized planar fault energy (GPFE) on {112} planes.[37,45] Since DFT has been employed to calculate the relaxed GSFE on {110} and {112} planes in W,[36,42,46] in this paper, we first conduct DFT simulations using VASP[47–49] to calculate the relaxed GSFE on a {123} plane as well as the relaxed GPFE on a {112} plane. The projector augmented wave (PAW) method[50] is utilized within the density functional framework.[51] The Perdew-Burke-Ernzerhof[52] formulation of the generalized gradient approximation[53] is used with a standard PAW potential for W containing 12 valence electrons. The wavefunction partial occupancies are determined by the method of Methfessel and Paxton[54] using a smearing width of 0.2 eV. The cut-off energy for the plane-wave basis set is chosen to be 450 eV. A conjugate gradient method is used to relax atomic positions with an electronic convergence criterion of 10^{-5} eV and an ionic convergence is achieved when all forces are less than 0.02 eV/Å. Spin-polarization was tested and found to be negligible.

Initially, supercells are created and rotated such that the glide is along the x direction on the x-y plane. These structures, each containing 36 atoms, are then relaxed fully for atomic positions, cell size, and cell shape. A vacuum region of 12 Å is then added to each supercell, creating a series of non-interacting slabs in the simulation region due to the periodic boundaries of the simulation box. Gamma centered k-point meshes of $15 \times 2 \times 1$ and $15 \times 9 \times 1$ are used for the {123} GSFE and the {112} GPFE, respectively. To obtain the relaxed GSFE curve, the top half of the cell is shifted incrementally in the x direction, holding the top two and bottom two layers fixed while allowing for relaxation of the inner 8 layers in the z direction only. A similar method is used in the relaxed GPFE curve calculation, except that 6 atoms, rather than layers, are held fixed on the top and bottom while the remaining 30 atoms are allowed to relax in the z direction, as the shifts are applied.

To assess the accuracy of both EAM and AT potentials, we calculate the same fault energy curves using molecular statics simulations[55–57] and benchmark them against the DFT results. Note the lattice parameter $a_0 = 3.14339$ Å and 3.1652 Å for EAM and AT potentials, respectively. Figure 1(a) suggests that at the interplanar displacement of one partial dislocation $\mathbf{b}_p = (a_0/6)\langle 111 \rangle$, both potentials predict that {112} planes have the highest SFE while {110} planes the lowest, in agreement with BCC Fe.[58,59] This suggests that dislocation slip on {110} planes is the most prevalent among the three sets of slip planes using these two potentials. The DFT calculations, however, predict that {112} and {123} planes have the highest and the lowest SFE, respectively. In addition, the TB migration energy, which is the difference between the unstable twinning energy γ_{ut} and the stable twinning energy γ_t, is about 5.5%γ_t (EAM), 0.8%γ_t (AT), and 2.1%γ_t (DFT), respectively, as shown in
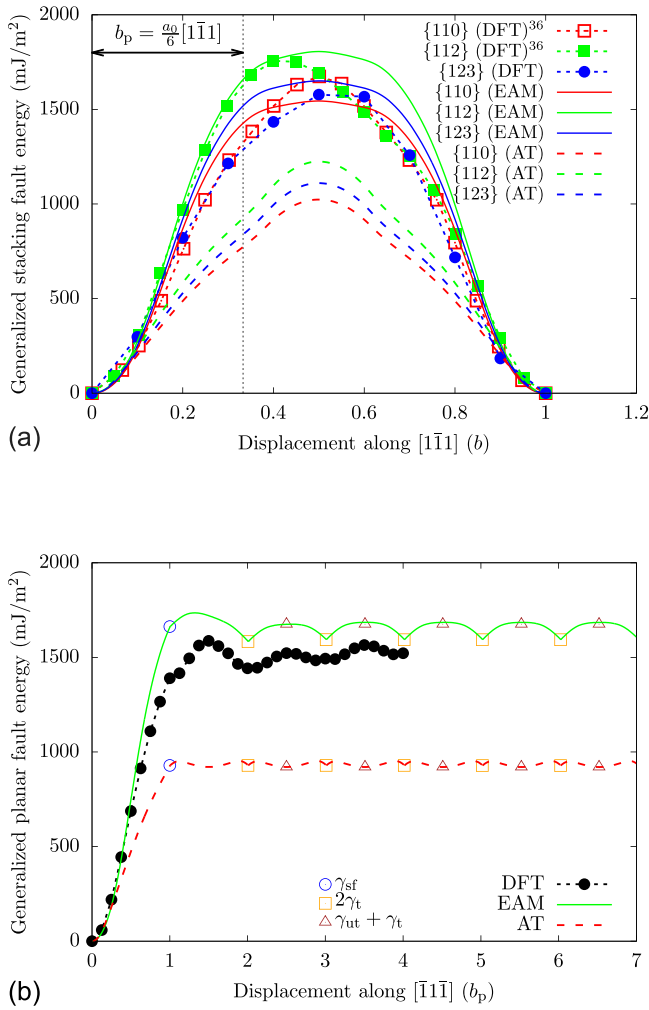
FIG. 1. (a) Relaxed GSFE on {110}, {112}, and {123} planes along the [1$\bar{1}$1] direction. b and b_p are the magnitudes of a full dislocation $\mathbf{b} = (a_0/2)$ [$\bar{1}$1$\bar{1}$] and a partial dislocation $\mathbf{b}_p = (a_0/6)[\bar{1}1\bar{1}]$, respectively, where a_0 is the lattice parameter. DFT data on {110} and {112} planes are from Ref. 36. (b) Relaxed GPFE on a {112} plane along the [$\bar{1}$1$\bar{1}$] direction. γ_{sf}, γ_t, and γ_{ut} are the stable stacking fault energy, the stable twinning energy (also the TB energy), and the unstable twinning energy, respectively.

Figure 1(b). This indicates that TBs are more susceptible to migration using the AT potential.

We note that the AT potential was fit to the pressure-volume relation,[41] while the EAM potential was fit to the lattice constants, the cohesive energies, the elastic constants, the formation energies of a mono-vacancy, and self-interstitial atom defects with different orientations, as well as *ab initio* forces acting on atoms in liquid configurations.[42] In other words, neither potential was fit to the SFEs. Nevertheless, our results, along with those in the literature,[36,42] suggest that the EAM potential shows a good transferability in yielding more accurate GSFE and GPFE than the AT potential. For example, on {110} planes which are the major slip planes in W at low temperatures,[60,61] the SFE at the interplanar displacement $\mathbf{b}_p$ calculated by EAM and AT potentials has a relative error of 2% and 47%, respectively, with respect to the DFT result,[36] as shown in Figure 1(a). For the GPFE on a {112} plane, Figure 1(b) suggests that both the EAM potential and DFT yield unstable structures at displacements $1.5|\mathbf{b}_p|, 2.5|\mathbf{b}_p|$, and $3.5|\mathbf{b}_p|$; however, the AT potential predicts metastable

structures at these displacements. Note that similar metastable structures were found in BCC Mo using the FS potential[37] (the AT potential would give the same result because it only differs in the short range region[41]), in contrast to the DFT simulation result in Mo.[62] Besides the fault energies, the AT potential predicts that the FCC structure is not a local maximum but a saddle point along the Bain transformation pathway, at odds with the EAM potential and DFT calculations.[42] Therefore, the EAM potential[42] is considered to yield more accurate plastic deformation in BCC W and is employed in MD simulations in the remainder of this paper.

III. MD SIMULATIONS OF PLASTIC DEFORMATION OF A TWINNED BICRYSTAL AND TWINNED NANOPILLARS

MD simulations are performed using LAMMPS[63] to study plastic deformation in a twinned bicrystal (Section III A) and twinned nanopillars (Section III B), respectively. A Velocity Verlet algorithm with a time step of 2 fs is employed to update the atomic positions. Each model is first dynamically relaxed for 10 000 steps under isobaric zero stress conditions followed by an energy minimization; then, a homogeneous deformation is imposed by changing the volume of the simulation box during a dynamic run to minimize shock waves. A constant engineering strain rate $\dot{\varepsilon} = \pm 10^9 \, \text{s}^{-1}$ is applied along the z direction until the uniaxial engineering strain ε reaches ± 0.2. The uniaxial engineering stress σ is calculated following the Virial stress formulation. Lattice defects are identified by the centrosymmetry parameter (CSP)[64] and the adaptive common neighbor analysis (a-CNA).[65]

A. A twinned bicrystal

A twinned bicrystal containing a {112} coherent TB (CTB) otherwise free of defects is constructed by carefully specifying lattice orientations in the two grains, i.e., $x[110]$, $y[1\bar{1}1]$, and $z[1\bar{1}2]$ for the lower grain, and $x[110]$, $y[\bar{1}11]$, and $z[1\bar{1}2]$ for the upper grain, as shown in Figure 2(a). Periodic boundary conditions (PBCs) are applied along all directions. The simulation cell contains 6 711 708 atoms and has a size of 47.12 nm × 47.09 nm × 46.97 nm. An NPT ensemble is employed to maintain a constant temperature of 10 K and zero transverse stresses in the x-y plane during uniaxial deformation along the z direction. A W single crystal with lattice orientations of $x[110]$, $y[1\bar{1}1]$, and $z[1\bar{1}2]$ is also deformed in the same way to provide a reference. While tensile deformation in a W single crystal has been explored by DFT along certain lattice orientations,[66] this is the first MD work to investigate uniaxial deformation in a single crystal and a twinned bicrystal in W, to the best of our knowledge.

Stress-strain curves in Figure 2(b) show that for both the single crystal and the twinned bicrystal, the compressive loading has a higher strength than the tensile loading. Snapshots of atomic structures at the yield point are presented in Figures S1 (supplementary material) and 3, for the single crystal and the twinned bicrystal, respectively.

Under tensile loading, in a single crystal, full dislocations with Burgers vector $(a_0/3)\langle 111 \rangle$ are homogeneously
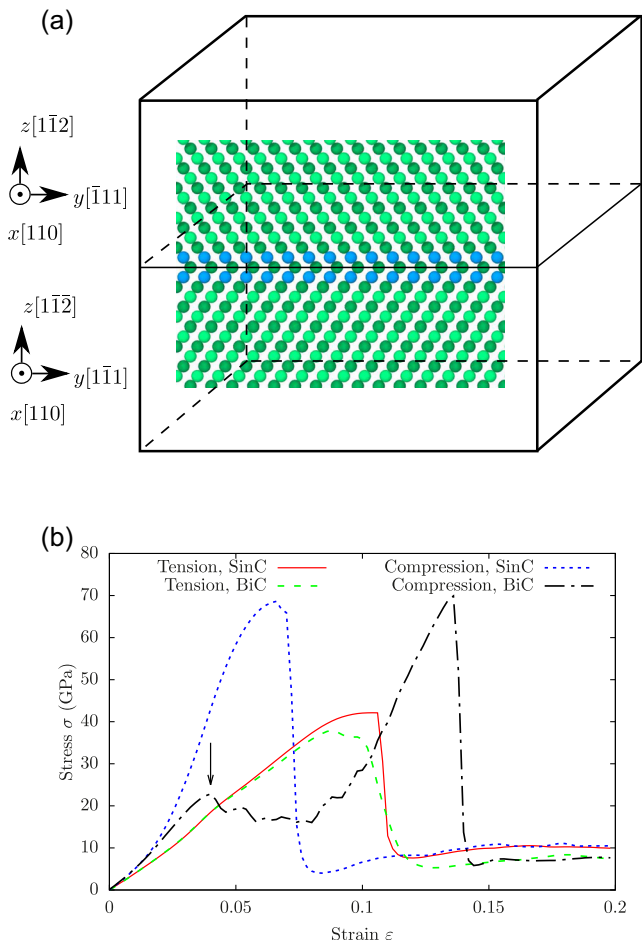
(a)

(b)

FIG. 2. (a) Simulation cell used to study plastic deformation of a twinned bicrystal in BCC W. It contains 6 711 708 atoms and has a size of 47.12 nm × 47.09 nm × 46.97 nm along the *x*, *y*, and *z* directions, respectively. (b) Stress-strain curves of the single crystal (SinC) and the twinned bicrystal (BiC) under tension and compression along the *z* direction. The first peak on the stress-strain curve of a twinned bicrystal under compression is pointed to by a black arrow and corresponds to the nucleation of the twinning-like planar defects in Figure S1(b) (supplementary material).

(a) Tension, $\varepsilon = 0.102$

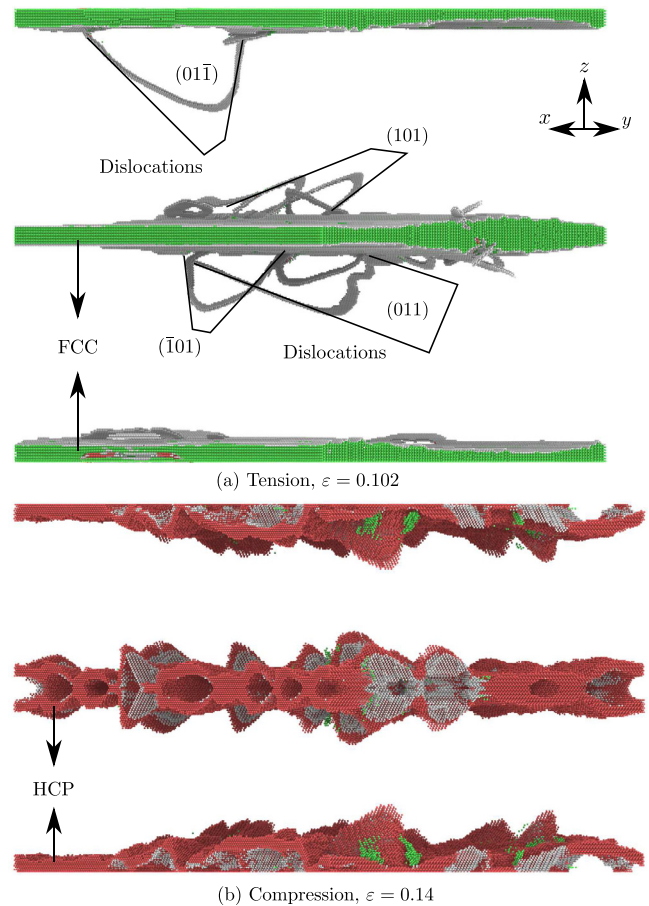(b) Compression, $\varepsilon = 0.14$

FIG. 3. Snapshots of atomic structures at the yield point in a twinned bicrystal under (a) tensile and (b) compressive loading. Atoms are colored by a-CNA:[65] green are FCC atoms, red are of HCP local structure, white are of unknown structures, and all BCC atoms are deleted.

nucleated on $(10\bar{1})$ and (011) planes (Figure S1(a), supplementary material), which have the same Schmidt factor of 0.41. As a result, the critical resolved shear stress is 17.15 GPa, close to the relaxed ideal shear stress (17.52 GPa) for homogeneous dislocation nucleation in the $\{110\}\langle 111\rangle$ slip system calculated by DFT.[67] In a twinned bicrystal, atoms in the vicinity of the TB undergo phase transformation from the BCC to the FCC structure. Then, full dislocations with Burgers vector $(a_0/3)\langle 111 \rangle$ on $\{110\}$ planes are nucleated from TBs, as shown in Figure 3(a). At higher strains, the FCC atoms are transformed back to BCC.

Under compressive loading, in a single crystal, some planar defects on $(3\bar{3}\bar{4})$ planes are homogenously nucleated upon yielding, as shown in Figure S1(b) (supplementary material). These defects, not residing on any known slip/twin planes but close to the $\{112\}$ twin planes, are a result of local lattice rotation, similar to the "twinning-like lattice reorientation" recently discovered in *in situ* compression of a submicron-sized single crystalline Mg pillar.[68] Note that (i) across the planes on which these planar defects are nucleated, no rational crystallographic orientational mirror

symmetry is established and (ii) these planar defects are nucleated at strain rates of 10^8–$10^9 \, \text{s}^{-1}$. At higher strains, dislocations on $\{110\}$ planes are nucleated from these defects to form a complex dislocation network. In a twinned bicrystal, the same planar defects are nucleated in the grain interior, albeit at a smaller strain than that for the single crystal, corresponding to the first peak stress (labeled by the black arrow in Figure 2(b)). At higher strains, these twinning-like planar defects disappear, and the stress continues increasing until approaching the second peak, when atoms near the TB begin to have HCP structures, as shown in Figure 3(b). Later, the HCP atoms are transformed back into BCC, and dislocations on $\{110\}$ planes are nucleated from the TB to form a complex dislocation network.

Our simulation result in the twinned bicrystal in BCC W is in contrast to that in FCC Cu under tensile loading[69] and in FCC Au under compressive loading,[11] in which dislocations are homogeneously nucleated in the grain interior instead of from TBs. This may be attributed to the fact that BCC W has a much higher CTB energy (796.8 mJ/m², see Figure 1(b)) than FCC Cu[70] (22.2 mJ/m²) and FCC Au[71] (21.7 mJ/m²). Moreover, the phase transformation, initiated at the TB in the twinned bicrystal, is not observed in the single crystal under either tensile or compressive loading. It will be shown in Section III B that the intermediate

twinning-like planar defects, but not the phase transformation, plays a role in plastic deformation of twinned nanopillars.

B. Twinned nanopillars

All twinned nanopillars have either a circular cross section (Figure 4(a)) or a square cross section (Figure 4(b)), with the same gauge length $L = 140.9$ nm. Lattice orientations in both grains are the same as in the twinned bicrystal. PBCs are applied along the central axis of the pillars, i.e., the z direction, while other surfaces are assumed traction free. The pillar cross section size D (edge length or diameter) ranges from 5 nm to 70 nm, resulting in models ranging from 178 791 to 44 487 302 atoms, respectively. We remark that the size of the largest model ($L = 140.9$ nm and $D = 70$ nm) is among the largest atomistic nanopillar models in the literature.[72] During uniaxial deformation, a Nosé-Hoover NVT integrator is used to maintain a constant temperature of 10 K. Single crystalline nanopillars with lattice orientations of $x[110]$, $y[1\bar{1}1]$, and $z[1\bar{1}\bar{2}]$ are also deformed in the same way to provide references.

The stress-strain curves of the twinned and single crystalline nanopillars with a circular cross section are presented in Figures 5 and S2 (supplementary material), respectively. For tensile loading, the yield point is defined as the initiation of lattice defects such as dislocations and twin embryos. Two cases exist for compressive loading: (i) without buckling, nanopillars are considered to yield when defects are nucleated prior to the global maximum stress along the stress-strain curves and (ii) in the presence of buckling, the global maximum stress is taken as the compressive elastic buckling strength. We emphasize that while yielding marks the material instability, buckling characterizes the structural instability. In the remainder of this paper, the threshold stress for both types of instability is referred to as the strength.

Snapshots of atomic structures with a circular cross section under tensile loading for the twinned and single

FIG. 5. Stress-strain curves of the twinned nanopillars with a circular cross section under (a) tensile and (b) compressive loading.

crystalline nanopillars are presented in Figures 6 and S3 (supplementary material), respectively. In the twinned nanopillars, at $\varepsilon = 0.076$, full dislocation loops with Burgers vector $(a_0/3)\langle 111 \rangle$ on {110} planes begin to nucleate from the TB/surface intersections: some dislocations glide into the grain interior while others along the TB plane. Unlike in the twinned crystal, the BCC $\rightarrow$ FCC phase transformation is not observed in the twinned nanopillars for all diameter D studied in this paper. Before yielding, the morphology of the nanopillars remains unchanged (Figure 6(e)); after the nucleation of dislocations, necking occurs near the TB region, and the nanopillars eventually fail by fracture along the TB plane (Figure 6(f)). In the single crystalline nanopillars, at the yield point, full dislocations with Burgers vector $(a_0/3)\langle 111 \rangle$ on (011) and $(10\bar{1})$ planes are nucleated from the pillar surface, forming slip bands, as shown in Figure S3(a) (supplementary material). At other sites of the pillar surface, partial dislocations emit on adjacent $(\bar{1}1\bar{2})$ planes, forming twin embryos, as shown in Figure S3(b). Then, instead of expanding into fully developed twin plates, the twin embryos produce full dislocation loops on {110} planes, in agreement with previous *in situ* TEM experiments.[18] Note that (i) the stress-strain curves for different pillar size D are similar for both single crystalline (Figure 5(a)) and twinned (Figure S2(a), supplementary material) nanopillars, and (ii) the size of the twin embryos nucleated from surfaces, which are not observed in the twinned nanopillars, decreases with D in the single crystalline nanopillars.
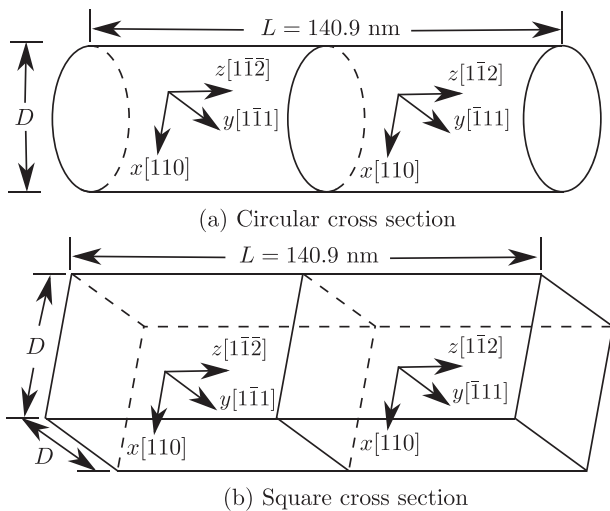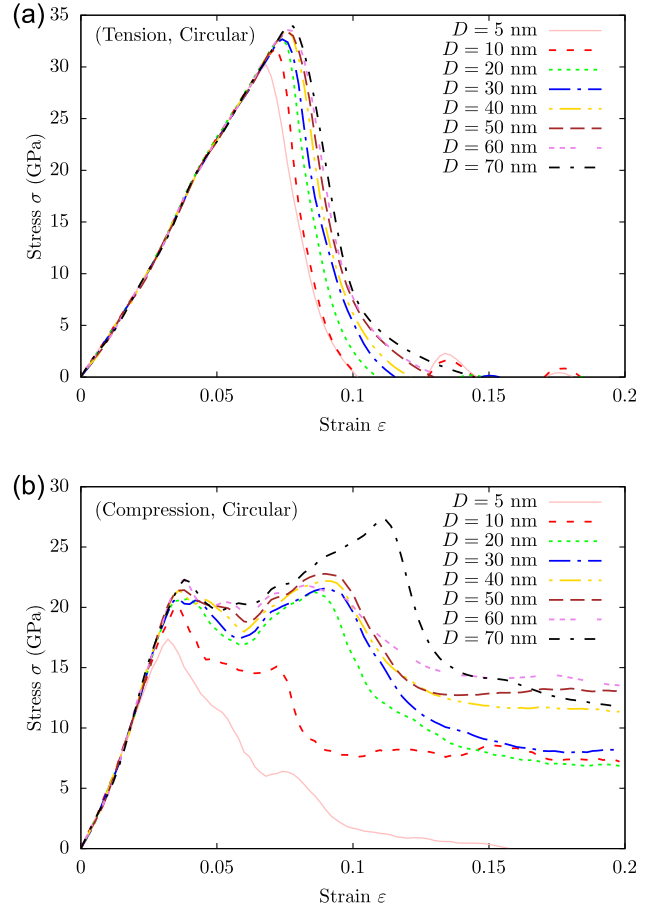

FIG. 4. Simulation cell of nanopillars with a (a) circular and (b) square cross section. With the same initial pillar length $L = 140.9$ nm, the initial size of the pillar cross section D ranges from 5 nm to 70 nm. The uniaxial loading is applied along the z direction.
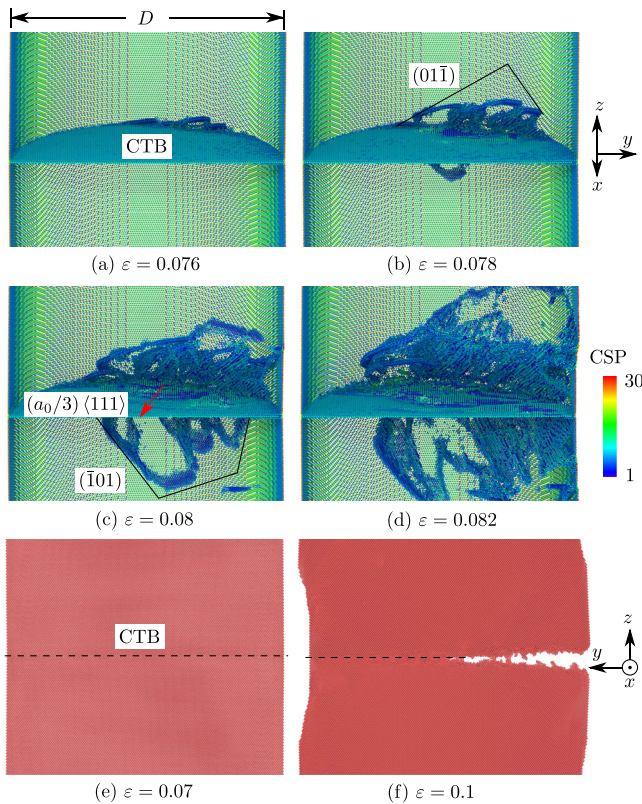
FIG. 6. Snapshots of atomic structures in the twinned nanopillar with a circular cross section ($D = 40$ nm) under tensile loading. In ((a)–(d)), atoms are colored by CSP;[64] those with a CSP smaller than 1 are removed. In ((a)–(d)), full dislocation loops with $(a_0/3)\langle 111 \rangle$ Burgers vector on {110} planes are nucleated from the intersections between the CTB and the pillar surface. CTB dislocations are marked by a red arrow in (c). (e) Before yielding, the morphology of the nanopillars remains unchanged. (f) After yielding, necking occurs near the CTB region, and the nanopillars eventually fail by fracture along the CTB plane. The CTBs in ((e)–(f)) are marked by dashed lines. Views in ((a)–(d)) and ((e)–(f)) are given near (b) and (f), respectively.
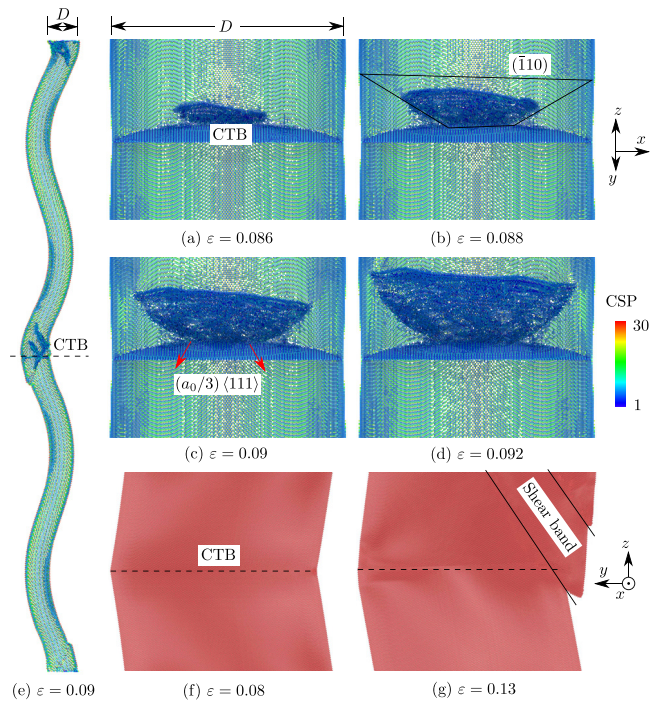

FIG. 7. Snapshots of atomic structures in the twinned nanopillar with a circular cross section under compressive loading. In ((a)–(d)) and ((f)–(g)), $D = 40$ nm; in (e), $D = 5$ nm. In ((a)–(e)), atoms are colored by CSP;[64] those with a CSP smaller than 1 are removed. In (a–e), dislocations on {110} planes are nucleated from the intersections between the CTB and the pillar surface, corresponding to the yielding in ((a)–(d)) and the threshold of plastic strain localization in elastic buckling in (e). CTB dislocations are marked by red arrows in (c). The CTBs in ((e)–(g)) are marked by dashed lines. Views in ((a)–(d)) and ((e)–(g)) are given near (b) and (g), respectively.

Snapshots of atomic structures with a circular cross section under compressive loading in the twinned and single crystalline nanopillars are presented in Figures 7 and S4 (supplementary material), respectively. The BCC → HCP phase transformation, which is exhibited in the twinned crystal, is not observed in the twinned nanopillars for all diameter D studied in this paper. Instead, the elastic compressive strain is accommodated by rotation of the lattice in each grain, as shown in Figure 7(f). At $\varepsilon = 0.086$, full dislocations with Burgers vector $(a_0/3)\langle 111 \rangle$ on {110} planes are nucleated from the TB/surface intersections and then glide either into the grain interior or on the TB plane, corresponding to the second peak stress (Figure 5(b)). As more dislocations are formed on adjacent {110} slip planes, slip bands are formed and greatly alter the pillar morphology, as shown in Figure 6(g). When $D = 5$ nm (i.e., the length-to-diameter aspect ratio is about 28), however, the nanopillar buckles at $\varepsilon = 0.034$, and the uniaxial stress begins to decrease. Figure 5(b) shows that there is only one peak on the stress-strain curve when $D = 5$ nm, differing markedly from those with a larger D, in agreement with previous finite element analyses.[73] Previous MD studies of single crystalline nanopillars in Au found that the buckling is common in nanopillars with a large aspect ratio and is affected by the lattice

orientation and the interatomic potential.[74–76] In our MD simulations, Figure 7(e) shows that the lateral displacement in the x-y plane (parallel to the TB) has a larger component along the y direction, normal to which the {111} plane has a higher surface energy, than the {110} plane, which is normal to the x axis; a similar displacement preference was also found in previous *in situ* TEM experiments in single crystalline nanopillars in Al with an aspect ratio larger than 6.[77] At $\varepsilon = 0.09$, dislocations on {110} planes are nucleated from the TB/surface intersections, corresponding to the threshold of plastic strain localization. In the single crystalline nanopillars, when $D = 5$ nm, the plastic strain localization is exhibited by nucleation of dislocation slip on {110} planes and twin embryos on {112} planes from sites on the pillar surface with the largest lateral y-displacement, as shown in Figure S4 (supplementary material). Similar to the tensile loading, the twin embryos do not expand to form full twin plates but serve as dislocation sources to produce full dislocations on {110} planes. In both single crystalline and twinned nanopillars, (i) the difference between the stress-strain responses for varying D is more pronounced in compressive loading than in tensile loading (Figures 5 and S2 (supplementary material)), (ii) when $D > 5$ nm, the buckling is negligible, and the twinning-like planar defects are nucleated in the grain interior, corresponding to the first peak on the stress-strain curves, and (iii) when $D = 5$ nm, the planar defects are not observed.

To investigate the effects of the pillar cross sectional shape, which was shown to play an important role in the deformation response of nanosized samples,[78] both single crystalline and twinned nanopillars with a square cross section (Figure 4(b)) are deformed in the same way as those with a circular cross section. We remark that while MD simulations of the effects of the pillar cross sectional shape have been conducted in FCC metals[79] and Si,[80] they have not been pursued in BCC metals, to the best of our knowledge. Figure 8 shows that full dislocations on {110} planes prefer to nucleate from the 90° corner which has a smaller activation volume than an atomically flat side.[81] Moreover, for the same cross section size D, nanopillars with a square cross section (Figure S5, supplementary material) have a lower strength, a lower flow stress at $\varepsilon = 0.2$, and a lower Young's modulus than those with a circular cross section (Figure 5), in agreement with previous MD simulations of single crystalline nanopillars in FCC Cu[79,81] and *in situ* experiments in single crystalline pillars in W.[61]

Figure 9 presents the strength σ_Y as a function of the nanopillar size D, in cases of tension/compression, circular/square cross section, and single crystalline/twinned nanopillars; values of σ_Y in the single/twinned crystals are plotted as references. It is found that for the same loading mode and pillar size D, (i) the twinned nanopillars have a lower strength than their single crystalline counterparts (due to the absence of the TB in the latter) and (ii) the strengths of the nanopillars are generally lower than those of the corresponding crystals. In comparison, *in situ* TEM experiments for W found that the strength of nanopillars, taken at 0.2% offset, is only about 2%–4% of the ideal strength.[82] In a recent high resolution TEM experiment of a bicrystalline nanopillar with a circular cross section ($D = 21$ nm) under [112] compression, the strength, taken when dislocations are simultaneously nucleated from multiple sources, is 17.56 GPa,[18] which is about 41% of the ideal strength. In addition, the

FIG. 9. Strength σ_Y as a function of nanopillar cross section size D, in cases of tension (T)/compression (C), circular/square cross section, and single crystalline (SinC)/twinned bicrystalline (BiC) nanopillar. Horizontal dashed lines are the strengths of a single or twinned crystal subject to different loading modes, distinguished by color.

shape of the stress-strain curves for nanopillars obtained by MD (in this work and elsewhere[17,22,79,83]) is very different from those measured in experiments.[21,23,44,61,82,84] In particular, significant strain hardening is present following yielding in experimental deformation of BCC pillars[85] but not in the corresponding MD simulations.[17,22] Therefore, it is difficult to extract the "flow stress" from the MD results in a manner consistent with that in experiments. However, we note that under compressive loading, the flow stresses at $\varepsilon = 0.2$ for the twined nanopillars (Figure 5(b)) are much higher than those for the single crystalline nanopillars (Figure S2(b), supplementary material). This suggests that, compared with their twin-free counterparts, the twinned nanopillars better resemble experimentally studied nanopillars which usually contain pre-existing dislocation sources.

When $D > 5$ nm, the present work in W and previous MD studies of single crystalline nanopillars in Fe[20,86] suggest that the strength σ_Y varies little with D, in contrast to experiments which revealed a log$D$ dependence of the strength for single crystalline BCC pillars.[82] For the same D, the strength is tension-compression asymmetric. Specifically, (i) in the single crystalline nanopillars, the compressive loading always has a higher σ_Y than the tensile loading, in agreement with previous *in situ* experiments of W single crystalline nanopillars under ⟨100⟩ loading,[82] and (ii) in the twinned nanopillars, the strength under compressive loading is lower than that under tensile loading. Note that the tension-compression asymmetry in BCC metals is mainly attributed to dislocations on {112} planes as opposed to those on {110} planes.[21] This explains why the asymmetry is more pronounced in the single crystalline pillars, where partial dislocations and twin embryos on {112} planes exist, than in the twinned pillars, where only full dislocations on {110} planes are nucleated.

It is useful to compare the MD simulation results in the literature with those based on experiments of nanopillars in BCC metals. To the best of our knowledge, (i) there is no experimental study of the twinned BCC nanopillars and (ii) with the exception of Ref. 18, most *in situ* TEM experiments

(a) Tension, $\varepsilon = 0.072$ (b) Tension, $\varepsilon = 0.08$

(c) Compression, $\varepsilon = 0.082$ (d) Compression, $\varepsilon = 0.092$
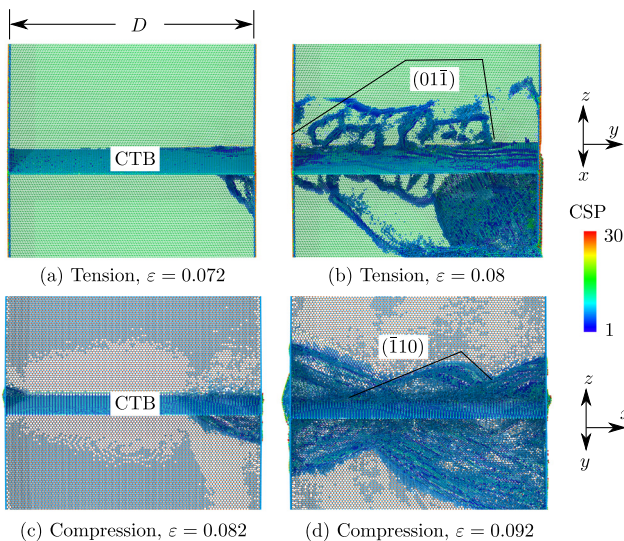
FIG. 8. Snapshots of atomic structures in the twinned nanopillar with a square cross section ($D = 40$ nm) under both tensile and compressive loading. Atoms are colored by CSP;[64] those with a CSP smaller than 1 are deleted. Dislocations on {110} planes are nucleated from the intersections between the CTB and the pillar surface.
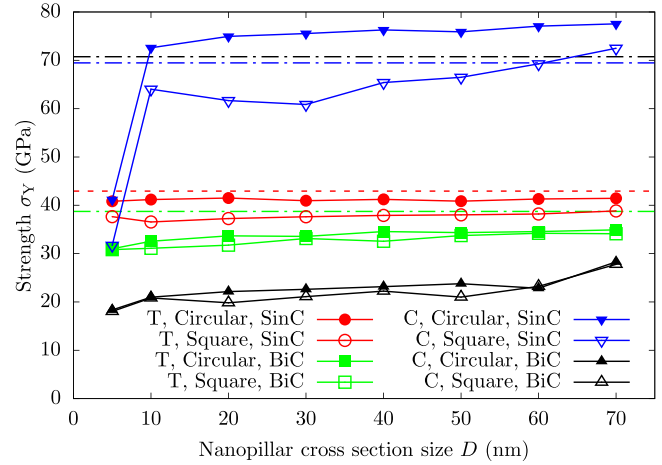
involve BCC nano/micropillars with a cross sectional diameter larger than about 100 nm. Therefore, only indirect comparisons in single crystalline or bicrystalline nanopillars can be made in BCC metals between MD simulations and experimental results. In W, Fe, Ta, and Mo, some MD simulations[37,83] in a wide range of temperatures (up to 1500 K) show that a $\langle 100 \rangle$-oriented nanopillar with a square cross section exhibits pseudoelastic mechanical twinning by a reversible twinning mechanism during tensile loading, in agreement with TEM measurements conducted on a $\langle 100 \rangle$-oriented W bicrystalline nanopillar at room temperature.[18] Other MD simulations in Fe, using different interatomic potentials, predict that the plastic deformation of $\langle 100 \rangle$-oriented nanopillars is dominated by dislocation slip[87] or phase transformation.[88,89] However, phase transformation has not been reported in any experimental work in Fe pillars. MD simulations for $\langle 110 \rangle$-oriented Fe nanopillars predict that the compressive plastic deformation is dominated by twinning[17] or phase transformation,[90] while only dislocation slip has been reported in experiments.[91–93] Clearly, there exist quantitative differences between MD simulations and experimental results in plastic deformation of nanopillars.

IV. CONCLUSIONS

In this paper, we first benchmark the fault energies predicted by two semi-empirical interatomic potentials against DFT calculations to shed light on the reliability of using these potentials to describe plastic deformation in BCC W. Then, the more appropriate potential, i.e., the EAM potential developed by Marinica *et al.*,[42] is employed to investigate tensile and compressive deformation of twinned nanopillars with different cross sectional shapes (circular or square) and sizes (5 nm to 70 nm) using large scale MD simulations. A single crystal, a twinned bicrystal, and single crystalline nanopillars are also studied as references. Stress-strain responses and defect nucleation/evolution are explored.

It is found that (i) in the single crystalline nanopillars, dislocation slip on {110} planes and twin embryos on {112} planes nucleated from the pillar surface dominate plastic deformation, (ii) in the twinned nanopillars, the onset of plasticity is exhibited by the nucleation of {110} dislocations from the TB/surface intersections, (iii) under compressive loading, both single crystalline and twinned nanopillars with cross section size $D = 5$ nm buckle, (iv) when $D > 5$ nm, the strength σ_Y exhibits a weak dependence on D under both tensile and compressive loading, (v) for the same cross sectional size/shape, a strong tension-compression asymmetry in σ_Y is exhibited in that the compressive strength is higher and lower than the tensile strength in the single crystalline and twinned nanopillars, respectively, (vi) for the same loading mode and D, the twinned nanopillars have a smaller tension-compression asymmetry and a higher flow stress than their twin-free counterparts, (vii) nanopillars with a circular cross section have a higher strength, a higher flow stress, and a higher Young's modulus than those with a square cross section, and (viii) the cross sectional shape of the nanopillars affects the initial sites of defect nucleation but not the overall stress-strain responses and defect nucleation.

While qualitative agreement is obtained between the present MD simulations and *in situ* TEM experiments, there exist quantitative differences that may be attributed in part to the much higher strain rate (10^9 s^{-1}) employed in MD compared to those ($10^{-3}-10^{-1} \text{ s}^{-1}$) in experiments,[94] as well as scarcity of dislocation sources other than the TB and the accuracy of the interatomic potentials used in MD. Future work includes employing time-scaling atomistic methods[95] to explore plastic deformation of twinned nanopillars at much lower strain rates and with a varying TB spacing.

SUPPLEMENTARY MATERIAL

See supplementary material for Figures S1–S5.

[1]L. Lu, Y. Shen, X. Chen, L. Qian, and K. Lu, Science **304**, 422 (2004).
[2]K. Lu, L. Lu, and S. Suresh, Science **324**, 349 (2009).
[3]L. Lu, X. Chen, X. Huang, and K. Lu, Science **323**, 607 (2009).
[4]X. Zhang, H. Wang, X. H. Chen, L. Lu, K. Lu, R. G. Hoagland, and A. Misra, Appl. Phys. Lett. **88**, 173116 (2006).
[5]A. Hodge, Y. Wang, and T. Barbee, Jr., Mater. Sci. Eng. A **429**, 272 (2006).
[6]A. M. Hodge, T. A. Furnish, A. A. Navid, and T. W. Barbee, Jr., Scr. Mater. **65**, 1006 (2011).
[7]Z. Wu, Y. Zhang, and D. Srolovitz, Acta Mater. **57**, 4508 (2009).
[8]L. Zhu, H. Ruan, X. Li, M. Dao, H. Gao, and J. Lu, Acta Mater. **59**, 5544 (2011).
[9]A. Stukowski, K. Albe, and D. Farkas, Phys. Rev. B **82**, 224103 (2010).
[10]J. R. Greer and J. T. M. De Hosson, Prog. Mater. Sci. **56**, 654 (2011).
[11]C. Deng and F. Sansoz, Mater. Res. Soc. Symp. Proc. **1049**, 141 (2007).
[12]C. Deng and F. Sansoz, Appl. Phys. Lett. **95**, 091914 (2009).
[13]C. Deng and F. Sansoz, Nano Lett. **9**, 1517 (2009).
[14]F. Hammami and Y. Kulkarni, J. Appl. Phys. **116**, 033512 (2014).
[15]Y. Zhang and H. Huang, Nanoscale Res. Lett. **4**, 34 (2008).
[16]L. Wang, F. Zhao, F. Zhao, Y. Cai, Q. An, and S. N. Luo, J. Appl. Phys. **115**, 053528 (2014).
[17]G. Sainath and B. K. Choudhary, Comput. Mater. Sci. **111**, 406 (2016).
[18]J. Wang, Z. Zeng, C. R. Weinberger, Z. Zhang, T. Zhu, and S. X. Mao, Nat. Mater. **14**, 594 (2015).
[19]C. J. Healy and G. J. Ackland, Acta Mater. **70**, 105 (2014).
[20]G. Sainath, B. K. Choudhary, and T. Jayakumar, Comput. Mater. Sci. **104**, 76 (2015).
[21]J.-Y. Kim and J. R. Greer, Acta Mater. **57**, 5245 (2009).
[22]G. Sainath and B. K. Choudhary, Philos. Mag. **96**, 3502 (2016).
[23]J.-Y. Kim, D. Jang, and J. R. Greer, Int. J. Plast. **28**, 46 (2012).
[24]A. S. Schneider, D. Kaufmann, B. G. Clark, C. P. Frick, P. A. Gruber, R. Mönig, O. Kraft, and E. Arzt, Phys. Rev. Lett. **103**, 105501 (2009).
[25]C. R. Weinberger and W. Cai, Proc. Natl. Acad. Sci. U.S.A. **105**, 14304 (2008).
[26]Y. Karasawa, T.-F. Mark Chang, A. Shibata, and M. Sone, Mater. Res. Soc. Symp. Proc. **1297** (2007).
[27]I. J. Beyerlein, X. Zhang, and A. Misra, Annu. Rev. Mater. Res. **44**, 329 (2014).
[28]Y. Zhang, P. C. Millett, M. Tonks, and S. B. Biner, Acta Mater. **60**, 6421 (2012).

[29]Y. M. Wang, A. M. Hodge, J. Biener, A. V. Hamza, D. E. Barnes, K. Liu, and T. G. Nieh, Appl. Phys. Lett. **86**, 101915 (2005).

[30]V. S. Boyko and R. Y. Kezerashvili, J. Phys. Chem. Solids **75**, 1119 (2014).

[31]Y. T. Zhu, X. Z. Liao, and X. L. Wu, Prog. Mater. Sci. **57**, 1 (2012).

[32]S. Xu, L. Xiong, Y. Chen, and D. L. McDowell, npj Comput. Mater. **2**, 15016 (2016).

[33]S. Xu, L. Xiong, Y. Chen, and D. L. McDowell, JOM **69**, 814 (2017).

[34]S. Xu, "The concurrent atomistic-continuum method: Advancements and applications in plasticity of face-centered cubic metals," Ph.D. thesis (Georgia Institute of Technology, 2016).

[35]S. Xu and Y. Su, Model. Simul. Mater. Sci. Eng. **24**, 085015 (2016).

[36]G. Bonny, D. Terentyev, A. Bakaev, P. Grigorev, and D. V. Neck, Model. Simul. Mater. Sci. Eng. **22**, 053001 (2014).

[37]S. Li, X. Ding, J. Deng, T. Lookman, J. Li, X. Ren, J. Sun, and A. Saxena, Phys. Rev. B **82**, 205435 (2010).

[38]S. Kotrechko, O. Ovsjannikov, N. Stetsenko, I. Mikhailovskij, T. Mazilova, and M. Starostenkov, Philos. Mag. **96**, 473 (2016).

[39]P. Villain, P. Beauchamp, K. F. Badawi, P. Goudeau, and P. O. Renault, Scr. Mater. **50**, 1247 (2004).

[40]M. W. Finnis and J. E. Sinclair, Philos. Mag. A **50**, 45 (1984).

[41]G. J. Ackland and R. Thetford, Philos. Mag. A **56**, 15 (1987).

[42]M.-C. Marinica, L. Ventelon, M. R. Gilbert, L. Proville, S. L. Dudarev, J. Marian, G. Bencteux, and F. Willaime, J. Phys.: Condens. Matter **25**, 395502 (2013).

[43]M. Mrovec, C. Elsässer, and P. Gumbsch, Philos. Mag. **89**, 3179 (2009).

[44]D. Jang, X. Li, H. Gao, and J. R. Greer, Nat. Nanotechnol. **7**, 594 (2012).

[45]J. A. Zimmerman, H. Gao, and F. F. Abraham, Model. Simul. Mater. Sci. Eng. **8**, 103 (2000).

[46]S. L. Frederiksen and K. W. Jacobsen, Philos. Mag. **83**, 365 (2003).

[47]G. Kresse and J. Furthmüller, Phys. Rev. B **54**, 11169 (1996).

[48]G. Kresse and D. Joubert, Phys. Rev. B **59**, 1758 (1999).

[49]P. E. Blöchl, Phys. Rev. B **50**, 17953 (1994).

[50]P. E. Blöchl, O. Jepsen, and O. K. Andersen, Phys. Rev. B **49**, 16223 (1994).

[51]P. Hohenberg and W. Kohn, Phys. Rev. **136**, B864 (1964).

[52]J. P. Perdew, K. Burke, and M. Ernzerhof, Phys. Rev. Lett. **77**, 3865 (1996).

[53]W. Kohn and L. J. Sham, Phys. Rev. **140**, A1133 (1965).

[54]M. Methfessel and A. T. Paxton, Phys. Rev. B **40**, 3616 (1989).

[55]A. Ojha, H. Sehitoglu, L. Patriarca, and H. J. Maier, Philos. Mag. **94**, 1816 (2014).

[56]S. Ogata, J. Li, and S. Yip, Europhys. Lett. **68**, 405 (2004).

[57]S. Xu, R. Che, L. Xiong, Y. Chen, and D. L. McDowell, Int. J. Plast. **72**, 91 (2015).

[58]D. Terentyev, A. Bakaev, D. V. Neck, and E. E. Zhurkin, Philos. Mag. **96**, 71 (2016).

[59]L. Ventelon and F. Willaime, Philos. Mag. **90**, 1063 (2010).

[60]C. R. Weinberger, B. L. Boyce, and C. C. Battaile, Int. Mater. Rev. **58**, 296 (2013).

[61]C. Marichal, H. Van Swygenhoven, S. Van Petegem, and C. Borca, Sci. Rep. **3**, 2547 (2013).

[62]S. Ogata, J. Li, and S. Yip, Phys. Rev. B **71**, 224102 (2005).

[63]S. Plimpton, J. Comput. Phys. **117**, 1 (1995).

[64]C. L. Kelchner, S. J. Plimpton, and J. C. Hamilton, Phys. Rev. B **58**, 11085 (1998).

[65]A. Stukowski, Model. Simul. Mater. Sci. Eng. **18**, 015012 (2010).

[66]Y.-L. Liu, H.-B. Zhou, Y. Zhang, S. Jin, and G.-H. Lu, Nucl. Instrum. Methods Phys. Res., Sect. B **267**, 3282 (2009).

[67]S. Ogata, J. Li, N. Hirosaki, Y. Shibutani, and S. Yip, Phys. Rev. B **70**, 104104 (2004).

[68]B.-Y. Liu, J. Wang, B. Li, L. Lu, X.-Y. Zhang, Z.-W. Shan, J. Li, C.-L. Jia, J. Sun, and E. Ma, Nat. Commun. **5**, 3297 (2014).

[69]Y. Luo, Y. Wang, Y. Wang, Y. Wang, and M. Sui, J. Mater. Sci. Technol. **25**, 211 (2009).

[70]Y. Mishin, M. J. Mehl, D. A. Papaconstantopoulos, A. F. Voter, and J. D. Kress, Phys. Rev. B **63**, 224106 (2001).

[71]G. Grochola, S. P. Russo, and I. K. Snook, J. Chem. Phys. **123**, 204719 (2005).

[72]X. W. Gu, C. N. Loynachan, Z. Wu, Y.-W. Zhang, D. J. Srolovitz, and J. R. Greer, Nano Lett. **12**, 6385 (2012).

[73]H. Zhang, B. E. Schuster, Q. Wei, and K. T. Ramesh, Scr. Mater. **54**, 181 (2006).

[74]E. Rabkin, H. S. Nam, and D. J. Srolovitz, Acta Mater. **55**, 2085 (2007).

[75]W. Jiang and R. C. Batra, Acta Mater. **57**, 4921 (2009).

[76]P. A. T. Olsson and H. S. Park, Acta Mater. **59**, 3883 (2011).

[77]R. J. Milne, A. J. Lockwood, and B. J. Inkson, J. Phys. D: Appl. Phys. **44**, 485301 (2011).

[78]S. Brinckmann, J.-Y. Kim, A. Jennings, and J. R. Greer, Int. J. Multiscale Comput. Eng. **7**, 187 (2009).

[79]A. Cao and E. Ma, Acta Mater. **56**, 4816 (2008).

[80]Z. Yang, Z. Lu, and Y.-P. Zhao, J. Appl. Phys. **106**, 023537 (2009).

[81]T. Zhu, J. Li, A. Samanta, A. Leach, and K. Gall, Phys. Rev. Lett. **100**, 025502 (2008).

[82]J.-Y. Kim, D. Jang, and J. R. Greer, Acta Mater. **58**, 2355 (2010).

[83]A. Cao, J. Appl. Phys. **108**, 113531 (2010).

[84]J.-Y. Kim, D. Jang, and J. R. Greer, Scr. Mater. **61**, 300 (2009).

[85]S. Brinckmann, J.-Y. Kim, and J. R. Greer, Phys. Rev. Lett. **100**, 155502 (2008).

[86]G. Sainath and B. K. Choudhary, Mater. Sci. Eng. A **640**, 98 (2015).

[87]Y. Zhang, D. J. Yu, and K. M. Wang, J. Mater. Sci. Technol. **28**, 164 (2012).

[88]L. Sandoval and H. M. Urbassek, Nano Lett. **9**, 2290 (2009).

[89]L. Sandoval and H. M. Urbassek, Appl. Phys. Lett. **95**, 191909 (2009).

[90]J. Zhu and D. Shi, J. Phys. D: Appl. Phys. **44**, 055404 (2011).

[91]B. R. S. Rogne and C. Thaulow, Philos. Mag. **95**, 1814 (2015).

[92]R. Huang, Q.-J. Li, Z.-J. Wang, L. Huang, J. Li, E. Ma, and Z.-W. Shan, Mater. Res. Lett. **3**, 121 (2015).

[93]A. B. Hagen, B. D. Snartland, and C. Thaulow, Acta Mater. **129**, 398 (2017).

[94]A. T. Jennings, J. Li, and J. R. Greer, Acta Mater. **59**, 5627 (2011).

[95]X. Yan and P. Sharma, Nano Lett. **16**, 3487 (2016).